Corrosion Science 190 (2021) 109630

Contents lists available at ScienceDirect

Corrosion Science

journal homepage: www.elsevier.com/locate/corsci

The speciation of niobium in the oxide layer of an irradiated Low-Tin ZIRLO nuclear material

J. Hawes [a,d], P. Warnicke [a], P. Burr [b], D. Ferreira Sanchez [e], D. Grolimund [e], J. Partezana [c], Y.-L. Chiu [d], S. Abolhassani [a,*]

[a] Laboratory for Nuclear Materials, Nuclear Energy and Safety, Paul Scherrer Institute, 5232, Villigen PSI, Switzerland
[b] School of EE&T, University of New South Wales, Sydney, NSW, 2052, Australia
[c] Westinghouse Electric Company, Pittsburgh, PA, 15235, USA
[d] School of Metallurgy and Materials, University of Birmingham, B15 2TT, Birmingham, United Kingdom
[e] MicroXAS Beamline, Paul Scherrer Institut, 5232 Villigen PSI, Switzerland

ARTICLE INFO

Keywords:
Irradiated
Zirconium based fuel cladding
Hydrogen uptake
XANES
XRD
Niobium

ABSTRACT

In this study the oxidation state of niobium, within the oxide layer of a low-tin ZIRLO[1] irradiated in a nuclear reactor, is examined using synchrotron. The unique set up allows simultaneous acquisition of X-ray florescence (XRF) and X-ray diffraction (XRD) maps. A gradual oxidation and evolution of niobium is observed and quantified which is then compared with the information on the distribution of oxide phases revealed by XRD. The results are discussed with the aim to better understand the hydrogen uptake mechanism for this material, particularly the cause of the increased resistance to hydrogen uptake seen in niobium containing alloys.

1. Introduction

Zirconium alloys are used as nuclear materials particularly because of their good corrosion resistance and low neutron capture cross section. As time in reactor increases, components in contact with liquid coolant (H_2O *or* D_2O) will form an oxide on the outer (waterside) surface. Alloying elements have been added to improve corrosion performance and lower hydrogen uptake. Some of these alloying elements, in particular if they have a low solid solubility in zirconium, will form intermetallic or secondary phases particles (SPPs), and provide anodic protection for oxidation [1] since the alloying elements are more electronegative than Zr. It is crucial that a protective oxide is maintained to prevent breakaway (rapid) oxidation. It has been observed in the past that some of these SPPs show a delayed oxidation in the oxide, and may contribute to the enhanced resistance to rapid corrosion [2].

Oxidation behaviour and hydrogen uptake can vary greatly with even small changes to alloying element composition and distribution. A particular interest in Nb exists as the Nb containing alloys show a lower hydrogen uptake [3–8] compared to Zr-Sn alloys like Zircaloy-2 used in the boiling water reactors (BWR) and Zircaloy-4 used in pressurised water reactors (PWR) [8].

Couet et al. [9] theorised that alloying elements such as Nb and iron (Fe) could lower the hydrogen pickup fraction (HPUF) for zirconium based cladding material, if found in an oxidation state less than (4+). The theory suggests that this would compensate for space charge in the oxide and increase the mobility of electrons, from the inner metal-oxide interface, across the oxide to reduce H^+ ions formed at the coolant-oxide interface, or at a distance far from the metal-oxide interface. Hence, the amount of H^+ reaching the underlying metal would be reduced. Une et al. [10] suggested that Nb^{5+} would favour the creation of electronic defects causing an increase in the concentration of electrons. Therefore, if Nb^{5+} is found in the outer oxide the increase in electron concentration may enhance the reduction of H^+ ions dissociated from water at the oxide surface, suppressing the flux of hydrogen across the oxide layer and through the interface. Therefore, it could be assumed that these two aspects should act in parallel to reduce the HPUF in Zr-Nb alloys.

For this reason, there is a desire to understand the speciation of such alloying elements, particularly Nb, in the oxide layer [3,6,7,9,11–14]. Previous studies have shown that Nb precipitates remain predominantly metallic some distance into the oxide layer, i.e. Nb precipitates display delayed oxidation compared to the Zr matrix [2,3,15–17]. Once these SPPs are oxidised, Nb atoms could gain oxidation states of 2+, 3+, 4+

* Corresponding author at: Laboratory for Nuclear Materials, Nuclear Energy and Safety, Paul Scherrer Institute, 5232, Villigen PSI, Switzerland.
E-mail addresses: jonathan.hawes@psi.ch (J. Hawes), sousan.abolhassani@psi.ch (S. Abolhassani).

[1] ZIRLO is the trade name of a zirconium based alloy produced by Westinghouse Electric Company.

https://doi.org/10.1016/j.corsci.2021.109630
Received 17 February 2021; Received in revised form 11 May 2021; Accepted 11 June 2021
Available online 16 June 2021

Table 1
The chemical composition, heat treatment and irradiation of the low-tin ZIRLO that was studied during this work.

Material name	Fe (wt %)	Sn (wt %)	Nb (wt %)	Heat treatment	Burnup (MWD/kgU)	Cycles *
Low-tin ZIRLO	0.1	0.7	1.0	RXA (recrystallized/annealed)	63	3

* In this case one cycle is 18 months.

and 5+, and corrosion kinetics models have been developed based on the assumption that Nb retains an oxidation state below the fully oxidised 5+ when incorporated into the oxide [9]. It is thus believed that the oxidation state of Nb atoms has a direct impact on the oxidation and H uptake kinetics of Zr-Nb alloys. However, the speciation of Nb through the oxide still remains unquantified. Previous studies on Zr-Nb Alloys (Zr2.5%Nb, Zr1.0%Nb, Zr0.6%Nb, Zr0.5%Nb) had been undertaken at PSI [6,7]. Those studies although confirming a variability of speciation, could not conclude a well-defined oxidation state for Nb (e.g. Nb^{2+}, Nb^{4+}or Nb^{5+}) and hence a systematic spectroscopic study aiming at characterising the Nb speciation as a function of its position in the oxide layer of irradiated material is still lacking. Furthermore, other researchers have not yet demonstrated an unambiguous distribution of the different states [12,17–19]. It is well established that the oxidation of Zr occurs at the metal oxide interface so once an oxide has been formed on the metal surface, both oxidising and hydriding species must travel through the pre-existing oxide layer to reach the underlying metal-oxide interface, to continue the oxidation process [20,21]. Therefore, a spatially resolved study into the oxidation state of Nb across the formed oxide layer near the interface can considerably improve the understanding of the mechanism by which ingressing species can be transported to the underlying metal-oxide interface.

During this study a low-tin ZIRLO alloy, which was irradiated in a PWR, having an average burnup of 63 MWD/kgU provided by Westinghouse was examined by synchrotron radiation. Spatially resolved X-ray absorption near-edge structure (XANES) spectroscopy was used to explore this layer with the aim to accurately quantify the speciation of Nb as a function of distance from the metal-oxide interface.

Furthermore, the X-Ray Diffraction (XRD) of the oxide was measured in parallel, allowing determination of the phase fractions of tetragonal and monoclinic throughout the oxide. Froideval et al. performed XRD on another Nb alloy containing 2.5%Nb. They stated that the oxide had a "preferential monoclinic structure" but "a possible small amount of tetragonal structure being not totally excluded" [7]. Tetragonal phase in the oxide has been studied by several researchers by XRD and it was reported that the highest amount of tetragonal phase was found close to the metal-oxide interface being in the region of 8–15 % for the autoclaved alloys studied (in ZIRLO, Zircaloy-4, Zr-1%Nb, Zr-2.5%Nb) depending on alloy and sample [22–27]. Garner et al. studied the phase fraction of monoclinic to tetragonal oxide for a Zircaloy-4 material by TEM and electron backscatter diffraction [28]. In general, the distribution of these phases on a larger scale than that of TEM lamella could be of great value, as it has been stated that the TEM sample preparation could cause a stress relaxation and encourage a phase transformation from tetragonal to monoclinic ZrO_2. Such relaxation is expected to be less present in the current study (which could be considered as an intermediate dimension between bulk samples used previously in XRD and the TEM sample) owing to the larger thickness of the sample investigated. The tetragonal to monoclinic phase transformation is known to have an associated volume increase of (3–7 %) which leads to cracking and porosity in the oxide [28]. Thus, the presence of tetragonal will imply less cracks near the interface. A more porous oxide would decrease the diffusion distance and promote the ingress of the oxidising and hydriding species closer to the interface, hence speed-up corrosion and hydrogen uptake. This study aims to give better spatially resolved results concerning the ratio and placement of these two well-known phases across the oxide on an irradiated material.

2. Material and experimental

2.1. Material

During this study, a low-tin ZIRLO alloy used as guide tube provided by Westinghouse was examined. After 3 cycles irradiated in Millstone (here 1 cycle lasts 18 months), the average burnup was 63 MWD/kgU. The composition and radiation history of this material can be found in Table 1.

The segment was provided to the laboratory, already prepared by FIB. It had the following dimensions: thickness 2.6 μm, width 13.3 μm, and height approximately 8 μm of which 6.4 μm was finely polished. The full thickness of oxide was not included on this sample as the aim was to study the oxide close to the interface (that is the latest oxide layer formed). The minimum and maximum measured oxide thicknesses by

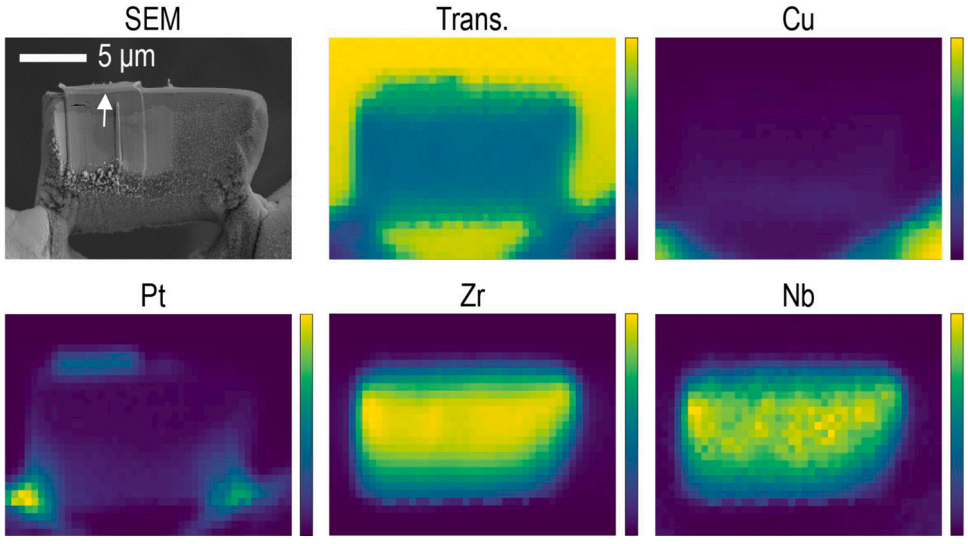

Fig. 1. X-ray fluorescence images of the low-tin ZIRLO sample (left to right): SEM image, transmission total, Copper signal, Platinum signal, Zirconium signal, Nb signal. The polished section can be clearly seen in the SEM image and this contains the analysed region which is roughly indicated by a white arrow.

SEM on this segment were 1.4 μm and 2.5 μm respectively, however the material had a full oxide thickness ranging between 10–12 μm. The reason to study the inner oxide is not only because this layer is the most recently formed oxide but also that the oxide in the vicinity of the interface is expected to dictate the further oxidation and hydrogen uptake properties of the material. Further details about the preparation of irradiated zirconium samples at their metal-oxide interface can be found in reference [29]. An SEM image of the studied sample can be seen in Fig. 1, along with other elemental signals from the Synchrotron campaign. The images show the borders of the sample by the Pt (deposited on the sample, during sample preparation, prior to FIB cutting) and Cu signals (from the copper grid on which the sample was mounted) which were used as markers during the campaign, as well as the major elements present in the sample. Although the beamline is capable of investigating radioactive materials by implementing temporary safety measures (e.g. shielding and radiation monitors at the end-station), the small size of sample had the benefit that the activity was low enough for the sample to be studied during standard (inactive) beamtime. For the purposes of this study the region probed for XANES was selected to contain the segment having as far as possible the maximum oxide thickness (indicated by the white arrow on Fig. 1).

2.2. Experimental

2.2.1. Acquisition of spectra

The synchrotron X-ray measurements were carried out at the X05LA/microXAS beamline at the Swiss Light Source (Paul Scherrer Institute, Switzerland). Monochromatic hard X-rays from the Si(111) double crystal monochromator of the beamline were focused down to approximately 0.8 μm (horizontal) ×0.7 μm (vertical) spot using a pair of Rh-coated Kirkpatrick-Baez (KB) mirrors. A graphic to show more exactly the beam size is included in the Appendix as Fig. A3. Fluorescent X-rays were measured using an energy-dispersive solid-state silicon drift detector (SDD, Ketek GmbH, Germany), oriented at grazing exit angle with respect to the sample surface. Chemical maps of the ZIRLO sample were obtained in the X-ray fluorescence mode using monochromatic X-rays with an incident energy of 19.1 keV. Micro-XANES spectra were measured also in fluorescence mode over the Nb K-edge. The XRD spectra were collected in parallel using an Eiger4M area detector (Dectris ltd, Switzerland).

In order to determine the speciation of Nb in the metal and in the oxide, a "point line-scan" was performed with the beam moving perpendicular to the metal/oxide interface from metal into the oxide with a predetermined step size of 200 nm. The step size has been selected to obtain a sufficient number of data points across the micron-sized sample, increasing the robustness of the analysis by over-sampling. Between two steps, in the case of XANES, an overlap of 70 % is present. The approximate distance, placement and direction are marked with a white arrow on Fig. 1. In the case of XANES, at each 200 nm interval, 10 spectra were acquired and averaged to improve statistics and reduce noise. Some of the spectra acquired had to be discarded due to obvious anomalies (related to pointing instabilities). For this reason, three of the spectra have a reduced statistics (they are the average of 7 or 8 spectra rather than 10). These spectra are located at 0 μm (metal-oxide interface), at 0.8 μm, and at 1.6 μm respectively. They are the 3rd, 7th, and the 11th in the row of spectra as will be reported in the results chapter. Overall, micro-XANES data have been recorded at 14 equally spaced locations, covering a total distance of 2.6 μm across the metal-oxide interface.

2.2.2. Data processing and standards used

Evolution of the Nb XANES signal when moving from metal to oxide was observed, to quantify this energy shift and shape change, standards with known speciation were used. It must be noted that three of the standards needed were directly acquired in the laboratory. However, the NbO (for Nb2+) and Nb_2O_3 (for Nb3+) were not available at the time of the measurements. To remedy the lack of these two standards, it was decided to obtain the corresponding reference spectra from other laboratories [3,30,31] and calibrate the spectra to match our acquisition conditions. The use of all five standards provides the most complete characterization of the XANES results. XANES scans were acquired for the following Nb standards: Nb metal, NbO (2+), Nb_2O_3 (3+), (Spectra for these standards: NbO (2+) [3], Nb_2O_3 (3+) [30,31], obtained from other laboratories) NbO_2 (4+) and Nb_2O_5 (5+). The resulting fluorescence spectra from each point in the line scan was fit using linear combination of these (normalised) standards using the Athena software and an in-house fitting Python script. The fit was based on minimising either the R^2 value or the root mean square error (RMSE) between the model and the measurement. The model spectrum is defined as

$$\mu_{model} = a\cdot\mu_{Nb^0} + b\cdot\mu_{Nb^{2+}} + c\cdot\mu_{Nb^{3+}} + d\cdot\mu_{Nb^{4+}} + e\cdot\mu_{Nb^{5+}} \quad (1)$$

Where μ_i represents the normalised spectrum of the i-th standard, with the constraints that the concentration of each standard in the model was between [0,1]

$$0 \le a, b, c, d, e \le 1$$

and that the sum of all standards added up to 1

$$a + b + c + d + e = 1$$

The portion of the spectra used for fitting the standards was in the energy range of 18950−19070 eV, which was chosen based on a sensitivity analysis provided in the Appendix. Fitting for R^2 and RMSE yield equivalent results.

As was previously mentioned, earlier results [6,7] reported an averaged oxidation state of Nb across the oxide layer. The procedure to acquire spectra at given distances from the metal-oxide interface, was used to obtain local information in the oxide. Still it appears that the measured spectra do not correspond to one single standard and thus are formed from a mixture of different Nb oxidation states even at a single point of inspection. In order to find out the relative fractions of each of the oxidation states the analysis described above was performed.

2.2.3. X-ray diffraction acquisition and analyses

X-ray diffraction patterns were acquired using an Eiger4M area detector, across the whole sample at intervals of 300 nm in both horizontal and vertical directions. The beam diameter was approximately 0.8 μm (horizontal) ×0.7 μm (vertical) as before for this data collection and the beam had an energy of 19.1 keV. It is worth noting that in the case of the XRD data points, there is 57 % overlap between two steps. The software XRDUA was used to analyse the resultant diffraction patterns and create semi-quantitative models of the phase fractions of the phases Zr, monoclinic ZrO_2 and tetragonal ZrO_2. For a more accurate calculation of the monoclinic vs tetragonal content in the oxide, specifically to account for the texture, the Garvie-Nicholson equation [32] was used. The expression is provided in Equation 2. Where I represents the intensity of the relevant peak i.e. $It - ZrO_2(101)$ represents the intensity of the tetragonal (101) peak. And R represents the phase fraction of tetragonal in the oxide.

$$R = \frac{I\,t - ZrO_2(101)}{I\,m - ZrO_2\left(\bar{1}11\right) + I\,t - ZrO_2(101) + I\,m - ZrO_2(111)} \quad (2)$$

The error on this expression was calculated using the general formula for error calculation [33] and is shown in Eq. (3). Here for simplicity x represents $I\,t - ZrO_2(101)$, y represents $I\,m - ZrO_2\left(\bar{1}11\right)$ and z represents $I\,m - ZrO_2(111)$. Δx, Δy, Δz represent the errors on x, y, z respectively.

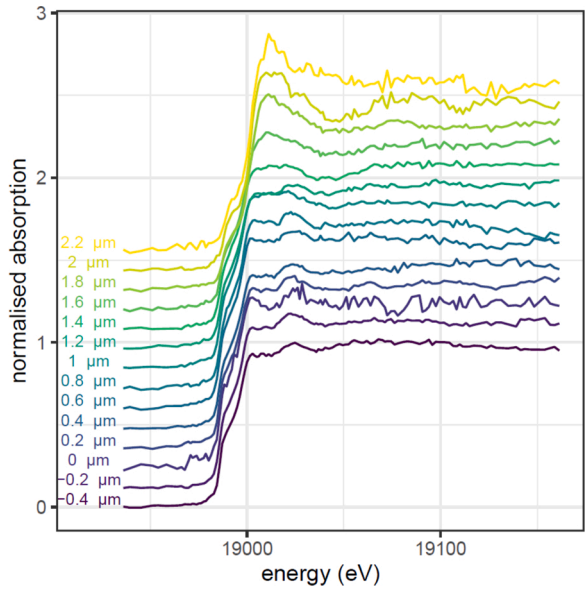

Fig. 2. Nb X-Ray absorption spectra moving from the metal into the oxide with a step size of 200 nm. All spectra have been normalised, and are offset vertically by 0.125 for ease of viewing. Three points have reduced statistics of 7 or 8 spectra averaged rather than 10. These points were the 3rd, at 0 μm (metal-oxide interface), 7th, at 0.8 μm, and the 11th, at 1.6 μm.

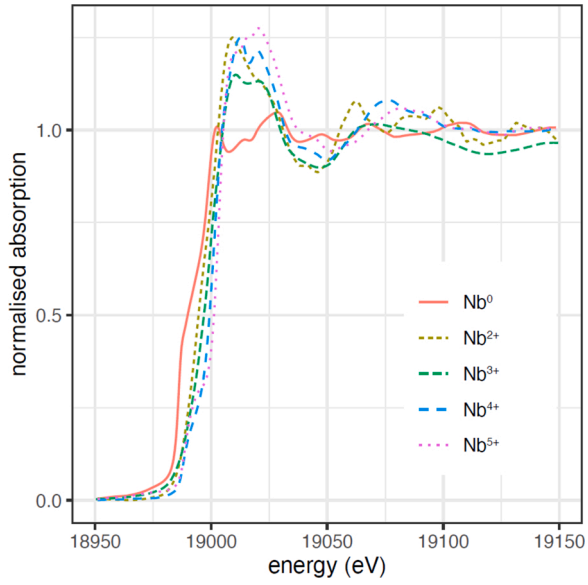

Fig. 3. Five XANES standards used for linear combination fitting. The five standards are Nb foil (metallic), NbO, Nb_2O_3 NbO_2, Nb_2O_5. All spectra have been normalised. The spectra for NbO and Nb2O3 were obtained from [3, 30,31].

$$error = \sqrt{\left(\frac{y+z}{(x+y+z)^2}\Delta x\right)^2 + \left(\frac{-x}{(x+y+z)^2}\Delta y\right)^2 + \left(\frac{-x}{(x+y+z)^2}\Delta z\right)^2} \quad (3)$$

3. Results

In the following, results of XANES acquisition and data processing will be reported first and subsequently the X-ray diffraction results will be provided.

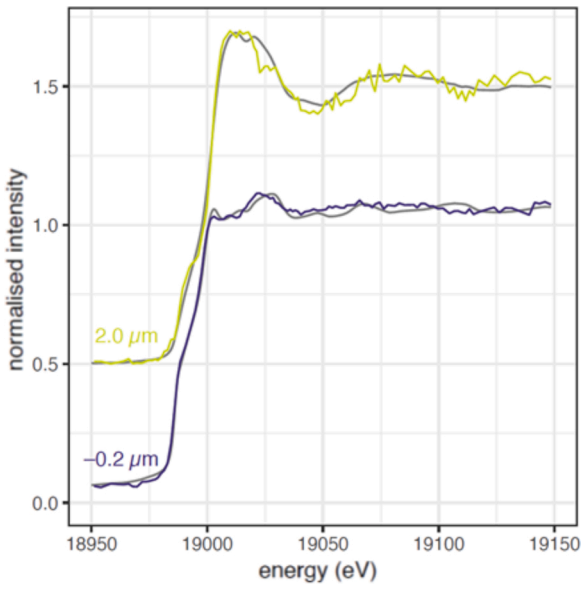

Fig. 4. Examples of linear combination fitting, where the coloured lines represent the spectra (as per Fig. 2) and grey lines represent the linear combination fit. The lower fit represents the metal part of the sample and the upper spectrum is taken 2 μm into the oxide. The results from the fitting for each point (i.e. each average spectrum), including these two, are provided in Fig. 5.

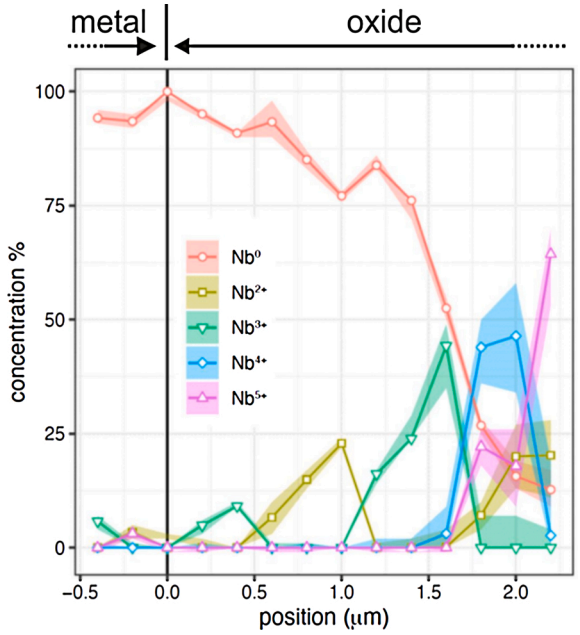

Fig. 5. The resulting constituent percentages for each position across the sample. The lines and points show the best linear combination fitting of the five reference standards. The shaded area represents the variation in fit when considering all solutions with residual error within 0.1 % of the best fit.

3.1. XANES of Nb

As the photon beam moves from metal across the metal-oxide interface and subsequently further into the oxide, the XANES signal shows a clear shift both in edge energy and in white line intensity. The averaged Nb absorption spectra from each point on the sample can be seen in Fig. 2. The displayed spectra have a spatial separation of 200 nm. The first spectrum has a position of 400 nm away from the interface located in the metal and the last spectrum is 2.2 μm away from the

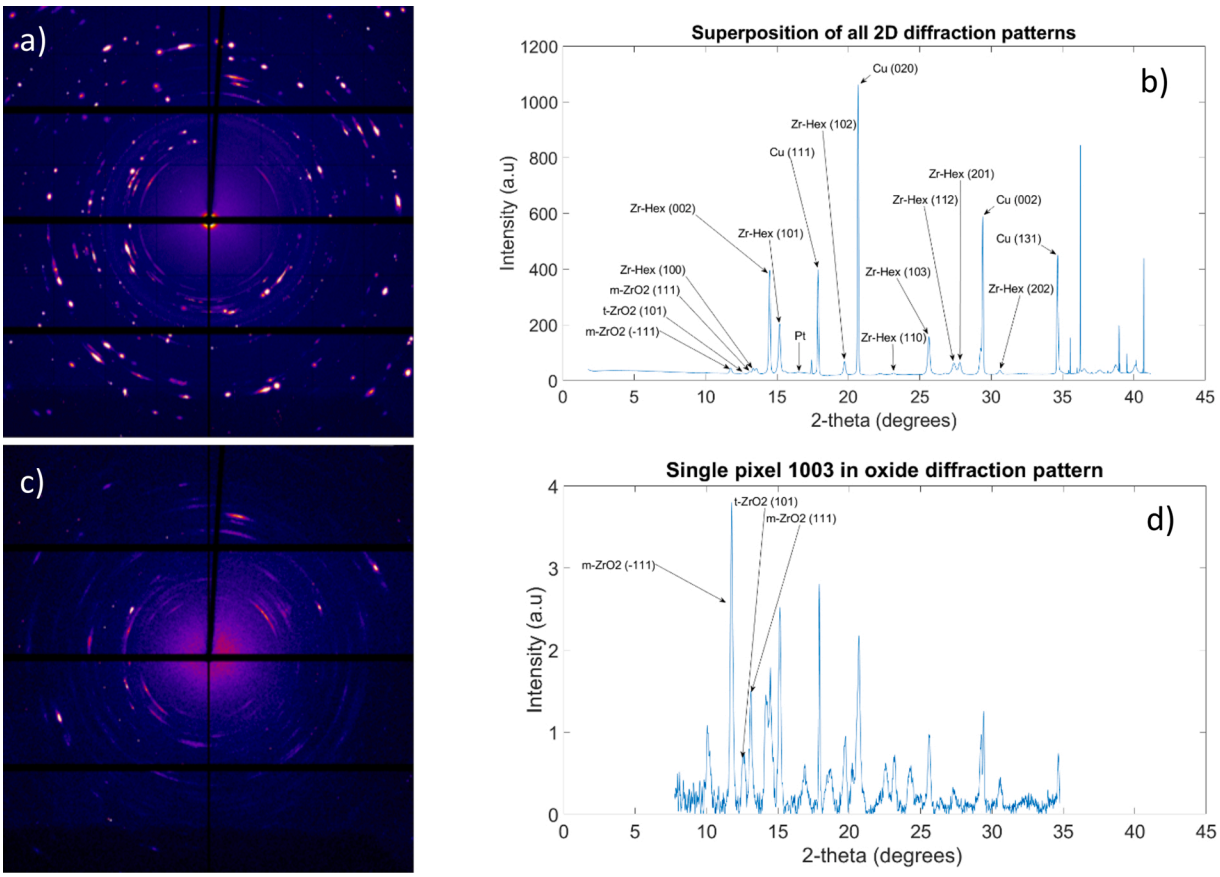

Fig. 6. a) Superposition of all 2D diffraction patterns from each 300 nm x 300 nm pixel. b) the resultant 1D spectrum which is a supposition of all diffraction patterns taken over the sample. Here the background has been removed. The copper signal originates from the copper grid used as sample holder, and is the most intense signal. The other phases are shown with annotation. c) The individual 2D diffraction pattern from one point of the sample in the oxide and d) the corresponding 1D spectrum from this single pixel.

interface in the oxide. The spectrum designated with 0 μm represents the metal-oxide interface, negative distances correspond to the metal and positive distances correspond to the oxide.

To quantify the evolution of spectra, as mentioned in Section 2.2.2, each spectrum was fit as a linear combination of Nb standards. The spectra of individual standards can be viewed in Fig. 3. This procedure allows to calculate the best mathematical fit from the given reference spectra, the percentage included from each standard corresponds to the percentage of Nb atoms in that state, i.e. metallic or different oxidation states. Examples of the resultant fits are shown for the XANES spectra in the metal and 2 μm into the oxide in Fig. 4. All five reference-spectra were included in the fitting for each point. The resulting percentages from the best fit for each spectrum, of the line scan, are displayed in Fig. 5. Once more, in Fig. 5 a distance of 0 μm represents the metal-oxide interface, negative the metal and positive the oxide. As expected in the metal portion of the sample the fitting shows Nb to be metallic, although it should be noted that the value from fitting is not 100 % metallic Nb, reasons for this are later discussed. Moving into the oxide Nb appears to slowly oxidise. At distances close to the interface, lower oxidation states are observed (2+ and 3+). However, somewhat counter intuitively small amounts of Nb^{3+} are seen in the first 400 nm of oxide and then larger amounts (approximately 25 %) of the Nb is seen as Nb^{2+} then more Nb^{3+}. After a distance of 1.2 μm into the oxide the metallic Nb begins to oxidise much more rapidly. A complex mixture of Nb oxidation states is seen in that region, with the general trend being Nb oxidising from Nb^{3+} to Nb^{4+} then finally to large amounts (over 50 %) of Nb^{5+} in the furthest point of oxide studied (in the 2 μm thickness region).

3.1.1. *Verification of fitting confidence*

Fitting the standards has a level of uncertainty associated with it, partly due to the signal to noise ratio of the measured spectra, and partly due to the effect of local atomic environment, which are different between the sample and the standards. While the local environment is not expected to affect the energy of the absorption edge, it may affect the structure of the spectra after the edge. To provide further confidence on the results presented above, the sensitivity of the results was tested against (a) the choice of spectral energy range used for fitting and (b) variations in the fitting parameters near the best-fit solution. Although (a) may lead to large uncertainties if the spectra are cut at values just beyond the edge, this uncertainty becomes vanishingly small when a suitably large spectral range is considered – see Appendix for details. On the other hand, (b) exploring the variations of fitting parameters near the best-fit solution provides an estimate of uncertainty caused by the noise in the signal. This is plotted as a shaded area in Fig. 5, which depicts the range of possible solutions that yield a residual error within 0.1 % of the best fit solution. More details are provided in the Appendix. This uncertainty is not constant throughout the oxide and at some points the uncertainty is higher, for example at 2.0 μm. However, it remains sufficiently small to provide confidence on the key findings.

As with any XANES analysis, there are additional sources of error that are not accounted for here which introduce noise into the data, these could arise from many sources such as; magnetic and electrical fields from equipment or elsewhere, cosmic rays or activity, beam instability, changes to the surrounding environment as well as others. This accounts for some of the uncertainty within these measurements and was previously mentioned as the signal to noise ratio. When observing the first 2 points in Fig. 5, these measurements are taken from

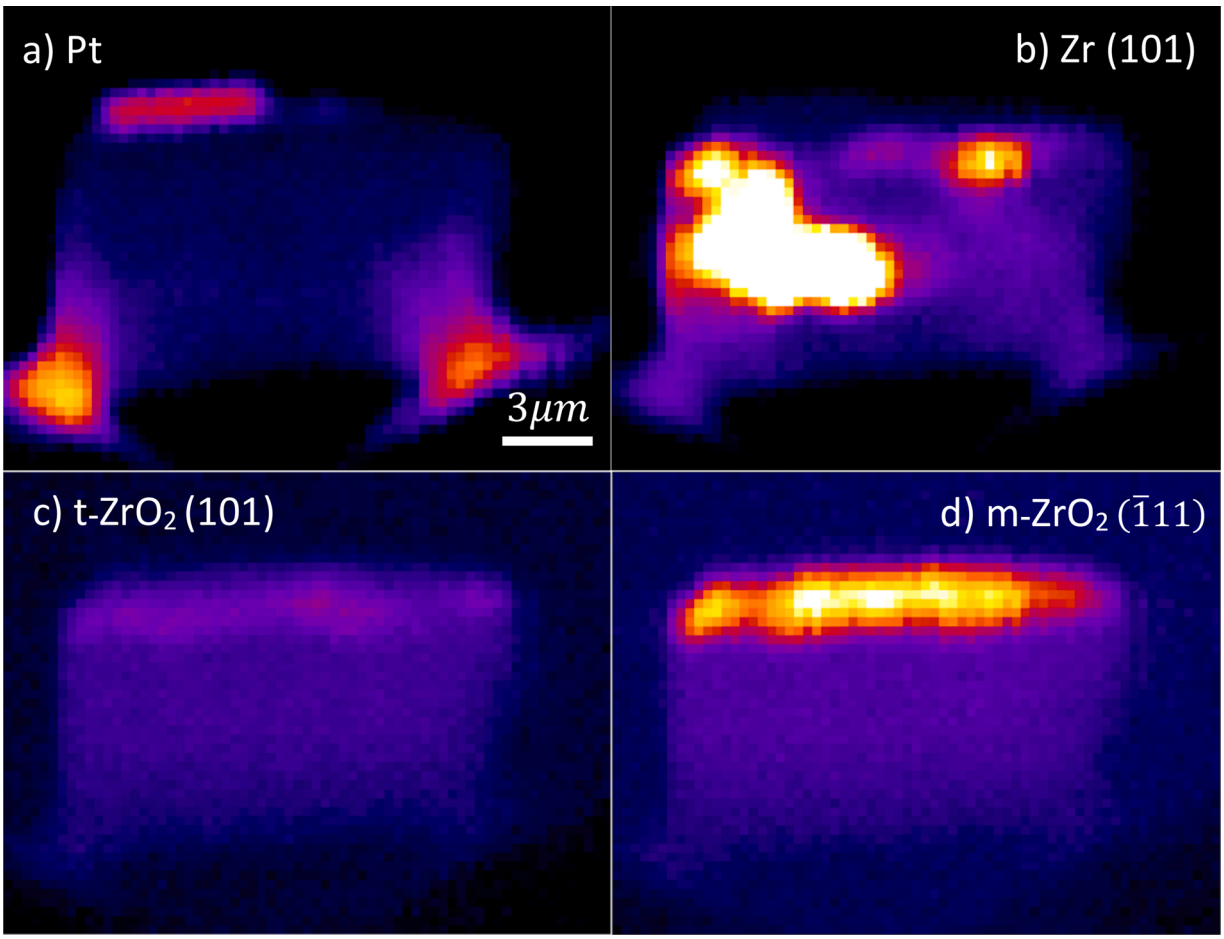

Fig. 7. a) Intensity map of XRD signal for platinum shown as a marker for the sample; to give the position and outline for intensity maps: b-d. b) Intensity map of XRD signal for Zr (101), c) for tetragonal ZrO_2 (101) peak and d) for monoclinic $\left(\bar{1}11\right)$ ZrO_2. Each pixel corresponds to one diffraction pattern and pixel size is 300 nm × 300 nm. A residual background observed on each map (the blue signal that depicts the profile of the specimen on each map) is left on the maps, for better visualisation of the contours of the specimen.

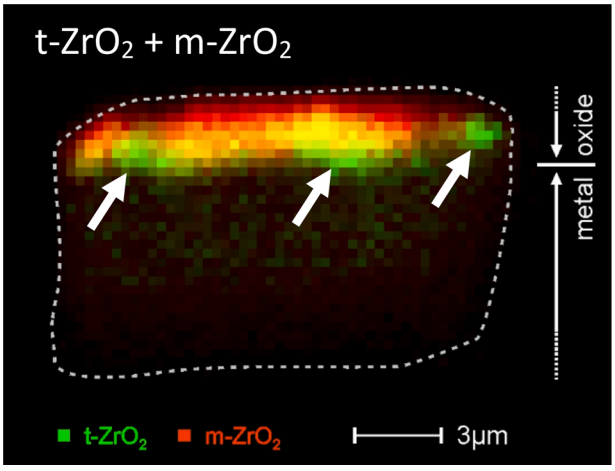

Fig. 8. Spatial distribution of Zr- oxide phases, obtained by superposition of the tetragonal and monoclinic maps from the Fig. 7 where the intensity scale is the same. Tetragonal ZrO2 (green), monoclinic ZrO2 (red), and yellow indicates the co-existence of both phases. Maximum red intensity indicates maximum concentration of monoclinic and maximum green intensity the tetragonal oxide. As observed, the tetragonal phase is observed to be preponderant close to the metal-oxide interface (white arrows). The dashed line indicates the contour of the sample. The interface between metallic Zr and oxide layer is indicated.

the metallic portion of the sample, and hence it may be expected that all of the Nb exhibits a Nb° charge state. However, the unconstrained fitting procedure obtains a lower residual error by including small additions (up to 5%) of the other standards. Furthermore, with the size of beam used for this experiment the tail of the beam will contribute to the signal, in this case it will be in the oxide which may account for the less than 100 % value of Nb°. The ultra thin 2−5 nm oxide formed on the surface of zirconium alloys even at room temperature could also contribute to this phenomenon. Nevertheless, these uncertainties appear to be small and do not reduce the trend of increasing oxidation state as the distance from the metal-oxide interface increases. Which is in line with expectations and in agreement with previously reported observations [6,7,12,17–19].

3.2. XRD results on monoclinic and tetragonal fractions

XRD patterns were taken with a step size of 300 nm in both the horizontal and vertical directions across the whole sample. This allows high spatial resolution XRD information across the whole sample to be taken and, in the case of this material, can provide the tetragonal and monoclinic phase fractions in the oxide. The superposition of all 2D diffraction patterns, can be seen in Fig. 6a and in Fig. 6b the resultant integrated 1D spectrum is provided as intensity vs 2θ. Furthermore, example of diffraction pattern from one pixel, in 2D and the 1D resultant are also provided in Fig. 6c and d. It must be noted that in Fig. 6b intense Cu peaks can be seen. The sample holder being made of Cu, some of the

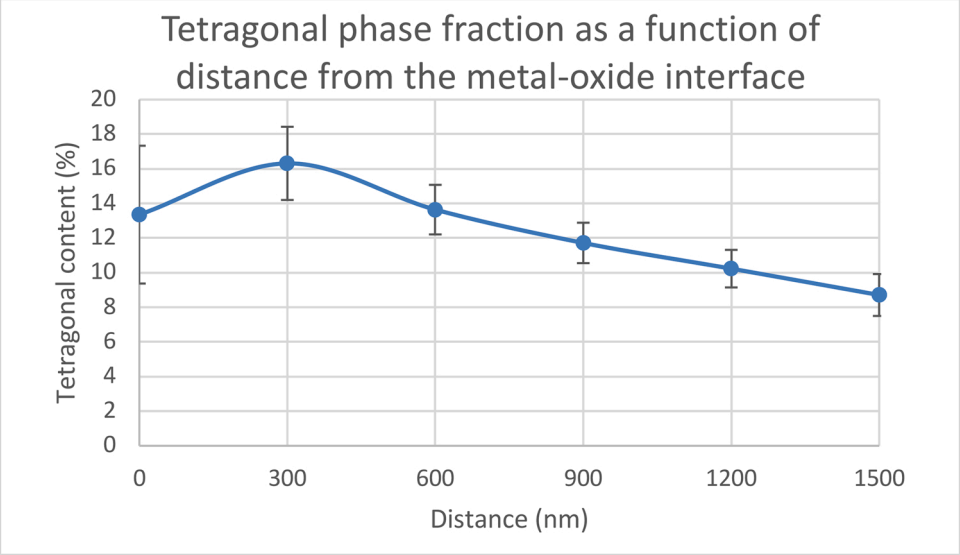

Fig. 9. The tetragonal phase fraction as a function of distance from the interface in the oxide, in the region close to the area studied for XANES. The interface is estimated to start at position of 0 nm on the graph.

pixels in the superposition presented in Fig. 6b included the peaks from the holder. Even when the beam is only on the sample, smaller peaks from Cu can be observed for example in Fig. 6d, due to the large amount Cu surrounding the sample compared to the sample itself. These peaks are not considered for the analysis.

The distribution of different orientations of phases over the sample can be observed in Fig. 7, which was obtained by selecting the intensity of one peak in every pixel of the map covering the whole sample. Texture exists in the metal part of the interface and regions with differently oriented grains can be viewed using this technique. For example Fig. 7b shows the intensity of Zr grains with the (101) orientation, showing 3 or 4 large textured grains in the metal. The tetragonal and monoclinic phases seen in the oxide side of the sample (Fig. 7c and d) are explored in more detail, with the aim to examine the tetragonal content as a function of distance from the interface.

In Fig. 8 the intensity of the two oxide phases are mapped together, tetragonal (101) as green and monoclinic $\left(\bar{1}11\right)$ as red. That means that the maximum green corresponds to the maximum tetragonal and maximum red to maximum monoclinic. However, maximum colour does not correspond to 100 % of respective phase. These maps are the superposition of. c and 7.d and are presented to provide a qualitative visual information about the spatial distribution of these phases in the oxide near the metal-oxide interface. It is therefore possible to distinguish the preponderance of tetragonal phase near the interface. In order to perform a quantitative analysis of the tetragonal content, the Garvie-Nicholson equation for tetragonal content was used [32]. The results of the quantification in the oxide are displayed in Fig. 9. Each data point is only one single XRD spectrum. This approach increases the accuracy and the resolution of the information. The calculation of error bars is shown in Section 2.2.3, and they are provided here to show the reliability of each data point. The values in Fig. 9 correspond to the phase fraction of tetragonal in the oxide, assuming that the only other oxide phase present is monoclinic ZrO_2. The possibility exists to take into consideration all signals, including the metal, to determine the ratios by creating a model from powder diffraction references, however due to the presence of texture the results would only be qualitative. Therefore, this calculation is not presented here and instead Fig. 9 is given. Due to the beam size, at the metal-oxide interface (distance 0 in Fig. 9) there will be some smearing of the data. This is reflected by the larger error bars due to the smaller signal to noise ratio at that point. The impact of this is that while the apparent maximum phase fraction of tetragonal is at 300 nm into the oxide it may be the case that similar amounts of tetragonal are seen in the first 300 nm; which is not evident from the data due to the smearing of information (between metal and oxide phases) collected at the interface. The undulating nature of the interface (and the fact that the interface is not planar) is also expected to add to this effect. Furthermore, due to the inhomogeneous nature of the material and the distribution of tetragonal at the interface (seen in Fig. 8), it must be expected that there will be some variation in the quantification of tetragonal. The area chosen for quantification in Fig. 9 was chosen to give the quantification in a similar region to that of the XANES study.

Two observations can be made; firstly, the highest amount of tetragonal phase is seen close to the metal-oxide interface; this has been reported previously from TEM [16,28] and Synchrotron [6,7,22–25] results. Secondly, the placement of tetragonal is not uniform parallel to the metal-oxide interface, instead what appears to be islands, or at least regions of higher intensity, of tetragonal can be seen and these do not appear to correspond with either areas of thick or thin oxide growth. These are marked with white arrows on Fig. 8.

4. Discussion

The aim of this work has been to study the speciation of Nb in the oxide layer of a ZIRLO alloy, near the metal oxide interface, to verify two points: i) is there any Nb_2O_5 present in the oxide? And ii) what is the exact speciation of the Nb as the distance from the metal-oxide interface increases? The interest for this information stems from the observation that in the case of Nb containing Zr alloys, the speciation of Nb influences the charge compensation near the interface and thus reduces the HPUF in these alloys [3,4,8,9]. According to the theories previously mentioned, this will only be the case if Nb is found in solid solution with an oxidation state of less than 4+ [9]. Therefore, the Nb 5+ state, if present, should be at a distance from the interface, for the above theory to be valid. The occurrence of Nb_2O_5 in the oxide layer, as well as its location is therefore of interest. Furthermore, the evolution of the Nb atoms' speciation with distance is of interest and is to be determined. As mentioned before, the presence of Nb_2O_5 at the water-side oxide has been reported by Une et al. [10]. These authors claimed that the presence of this phase near the outer oxide promotes the reduction of H^+ closer to the coolant and thus further reduces the ingress of hydrogen into the metal substrate.

The configuration of the experiment in the current study, from the point of view of the sample dimensions allows reflection and

transmission experiments. The geometry of the microXAS optics, and the resolution of the beam, permit the acquisition of spectra with a high resolution, in order to obtain clear answers to the above questions.

4.1. Scope and validity of results

In order to increase the resolution of acquisition the beam has been focused to obtain a sub-micrometre spot size (700 nm vertical by 830 nm horizontal). The step size has been selected to obtain a sufficient coverage of the sample, and the fact that the step size is smaller than the beam diameter, satisfies this full coverage of the space. In this manner between the two steps in the case of XANES, an overlap of 70 % is present and in the case of the XRD a 57 % overlap exists. Thus, the claim that the area scanned will be sufficiently covered and little information is missed out, is acceptable. Due to the beam size and convolution of features there is of course a certain smearing of the data at the interface between the metal and the oxide information, however, the phases present, and the multiple signals obtained in parallel have allowed to separate these regions from each other.

In this study, the need to acquire reference spectra from standards representing all possible oxidation states of Nb has been verified. At a first stage, due to the difficulties of procuring such chemical standards, the fitting of the spectra was performed using four standards, assuming that the Nb^{3+} standard can be omitted (please refer to Fig. A4 in the Appendix for comparison). However, the supply of Nb^{3+} spectra from other laboratories [30,31], allowed to recalculate percentages, and improved the confidence in the results. This allowed a better interpretation and understanding of the phenomena at the interface. It was concluded that the use of all five standards would clearly provide the most reliable fit for the spectra. Results showed that the Nb oxidation state evolves gradually from the lowest to the highest speciation at the first micrometres of oxide away from the metal-oxide interface.

The XRD results reveal the presence of tetragonal phase in the oxide. Due to the small concentration of the Nb oxides, these oxides could not yet be revealed in the data. Work is in progress to further analyse this aspect.

4.2. Delayed oxidation and metallic Nb in the oxide

From Fig. 5 it can be seen that the Nb in the oxide remains predominantly metallic until 1.2–1.4 μm into the oxide, after this there is a sharp change in gradient of the curve and Nb rapidly oxidises. The alloy examined, contains a certain amount of Sn in its composition, and thus it cannot be compared with the binary Zr-Nb alloys such as from ref [2]. The Nb concentration of 1.0 wt% implies however, that a certain number of SPPs are present and will show delayed oxidation. The finding that Nb remains metallic (in the SPPs) to these distances into the oxide layer is not new and is in good agreement with other studies on Nb alloys, both in irradiated state [16,34,35] as well as in autoclave [2,3,15,17]. However, if a part of this Nb is in solid solution, this is of importance.

Assuming that the results on Fig. 5 represent the real state of the material, an increase of metallic Nb at a distance of 1.2–1.4 μm is most likely explained by the presence of a larger number of SPPs in that area. It is suggested that a protrusion from the metal part in that region is very improbable, although it has been observed in other studies.

The observation that Nb retains mostly its metallic state in the vicinity of the metal-oxide interface, is interesting. It can be claimed that the Nb in the solid solution also remains partly metallic in the very early stages of oxidation. The solid solubility of Nb in the Zr matrix is in the range of 0.4 to 0.6 wt% depending on different types of alloys. It can be assumed in the case of the ZIRLO alloy, where approximately 0.5 wt% is claimed to be in the solid solution [25], the amount of metallic Nb should be much lower, if most Nb in solid solution would have immediately oxidised. To explain this more clearly, the signal at each point in the oxide, is from the entire Nb probed at that point, both from SPPs and matrix. Approximately 50 % of the signal should come from matrix and 50 % from SPPs, before they dissolve. If only the Nb in SPPs remained metallic the signal once in the oxide should give a much smaller metallic contribution. However, this is not the case. Therefore, it can be concluded that a part of Nb in matrix is also still in metallic state.

4.3. Nb oxidation state close to the metal-oxide interface

In this study, after approximately 0.5 μm into the oxide, certain amounts of Nb^0 are oxidised into Nb^{2+} then subsequently into Nb^{3+}. At a distance of 1.4 μm from the interface, the remainder of the Nb^0 signal starts to drop rapidly and is initially replaced by increasing amounts of Nb^{3+} which rapidly is replaced by Nb^{4+} and then Nb^{5+}. This has implications on the H transport kinetics, as Nb^{2+} and Nb^{3+} have been suggested to compensate for space-charge variation in the oxide during corrosion [9], resulting in parabolic oxidation kinetics and at the same time reduced HPUF [9]. The elimination of aliovalent dopants in the oxide (e.g. Nb^{2+} and Nb^{3+}), either through clustering effects [36–38] or by increasing the oxidation state to 4+ and 5+, leads to an increase in space-charge, which hinders the diffusion of oxygen vacancies in the protective oxide layer and result in a sub-parabolic oxidation kinetic [38]. However, in that case, it is claimed that the HPUF will increase.

The fact that aliovalent doping as described above, affects the kinetics of the HPUF is an important consideration. This latter is defined as:

$$\mathrm{HPUF} = \frac{\text{Hydrogen absorbed in cladding}}{\text{Hydrogen produced}}$$

In order to complete the electrochemical corrosion cell, charge must be transferred from the metal/oxide interface (anode) to the oxide/water interface (cathode). This is primarily achieved via electronic transport from the metal side through the oxide, towards the waterside, but can also be partially fulfilled by H^+ transport in the opposite direction. Thus, aliovalent dopants which increase the electronic conductivity of the protective oxide favour hydrogen recombination near the oxide/water interface, thereby reducing the HPUF [9,39].

It must be noted that due to the beam size of 0.71 × 0.83 μm, and the step size of 200 nm for the data points reported in Fig. 5, the data around the metal-oxide interface will have a small overlap between metal and oxide signals. Bearing in mind this factor, a more detailed analysis of Fig. 5 indicates two regions, a region starting from 0.4 μm into the oxide, where the oxidation state of Nb increases gradually from 2+ to reach around 2.2 μm to 5 + . Another region ahead of this latter can also be observed, starting from the interface to around 0.4 μm, where a small concentration of Nb^{3+} (starting from 0% and reaching to ca 10 % around 0.4 μm) exists.

In the region nearest to the interface, as the concentration of this Nb^{3+} oxide seems quite small, an uncertainty exists in its quantification and as previously explained the fitting procedure may often include small amounts of other phases to account for the deviation between the experimental spectrum and reference spectrum. However, some early oxidation of Nb at the metal-oxide interface is not surprising and could have two origins. The first one is the surface oxidation of the specimen which occurs even in air and is usually of the nanometre range although its thickness can vary depending on the oxidation properties, and the methods of preparation. The irradiated materials show a bigger tendency for such oxidation. The second origin of such signal is the oxidised Nb in the oxide matrix in that location. It would be expected that Nb in the oxide matrix had oxidised but since the values are not much higher than on the metal side of the interface, it is difficult to conclude with certainty. If some oxidation of Nb is present, its quantity is small with respect to the total content of metallic Nb present.

However, the distance of 0.4 μm, until 1 μm, shows mostly a 2+ speciation, which then is replaced by larger amounts of 3 + . The presence of Nb^{2+} has been observed in the TEM for the SPPs as well [35]. Furthermore, the first 1 μm of the oxide layer shows a gradual increase

of the Nb^{2+} and in parallel a drop of metallic Nb. These observations points towards gradual and partial oxidation of Nb present in the solid solution in the vicinity of the interface.

4.4. Nb oxidation state at a distance from the interface

Subsequently it seems that the Nb^{2+} drops at a distance of 1.2 μm and higher oxidation states appear. Two possible scenarios can describe this behaviour. One is that Nb gradually oxidises in the SPPs in the same way as the Nb in the oxide matrix from 2+ to 3+, 4+ and more. The other scenario could be that the scheme of oxidation totally changes. The gradual increase gives way to direct oxidation to 4+ and finally to 5+ with only small amounts oxidising first to 2 + . As the concentration of 2+ in the oxide does not increase considerably, the second scenario seems more plausible. It must be noted that at a specific distance from the metal-oxide interface, all Nb (both in the SPPs and that in the matrix), should be oxidized, and therefore, no further change should be observed above that distance.

The large amounts of Nb^{3+} and Nb^{4+} occurring after 1.4 μm may indicate the region where the oxide transitions from being protective to being porous and permeable. However, enough Nb^{2+} and Nb^{3+} is present to support the theory that Nb is present in a lower oxidation state than 4+ in the newest part of the oxide (i.e. close to the interface), which is expected to be the region of the oxide which is protective and acts as a diffusion zone to ingressing species.

A large quantity of Nb^{5+}, slightly over 50 % and significantly above the uncertainty limit, is observed at 2.2 μm into the oxide. This is of interest as there is still debate about the presence of this species near the interface, and its role on hydrogen pickup. Our findings evidence that at some distance from the metal/oxide interface, most of the Nb oxidises to the highest oxidation state. However, the transition to the 5+ oxidation state of Nb is occurring at a distance into the oxide that may be considered beyond the protective barrier layer, that is, in the porous monoclinic oxide that may not provide a rate-limiting barrier for further oxidation and H pick-up [40–42].

4.5. XRD results

The XRD data provides information about the crystal structure of zirconia that is to a certain degree in agreement with the results observed by other researchers. The oxide structure near the interface shows the presence of tetragonal ZrO_2. The highest amount of tetragonal is seen in the first point in the oxide with approximately 16 % of the oxide being tetragonal phase. The tetragonal content seems to decrease gradually with the distance from the interface. Due to the uncertainty about the signal intensities, it is not possible to explore the peaks at a distance of 2 μm from the interface (and beyond), owing to the size of the sample and the intensity of the peaks, which reduces gradually as the beam goes out of the sample and into the air. A certain periodic increase and decrease of tetragonal would be expected, as observed in other materials [22]. However, the maximum content of tetragonal phase is seen at 300 nm from the interface. Interestingly the tetragonal ratio is high in the region where the speciation of Nb in the oxide is mostly metallic, and the Nb2+ gradually starts to appear. It could be argued that the presence of metallic beta-Nb particles in this region (i.e. close to the metal-oxide interface), which are more compliant than the oxide, will accommodate the stresses in the oxide, close to the interface and will allow the existence of the tetragonal metastable phase. The sample examined in the present study, has only the inner 2.5 μm oxide however as mentioned the total oxide thickness of the segment after 3 cycles is in the range of 10–12 micrometres, thus, it can be assumed that the oxidation has passed the transition phase.

It must be mentioned that in this study, the zirconium monoxide (ZrO) observed quite often in autoclaved materials [43–49] but also as a thin layer on a similar neutron irradiated ZIRLO sample [35], has not been revealed. One reason for this could be the detection limit of XRD measurement in our setup (the ZrO revealed by that study [35] was in the range of 30–50 nm wide, extending from the metal to the oxide). It should be mentioned that while such ZrO phase has been often reported in autoclaved materials such reports are rare for irradiated materials [35].

5. Conclusions

The speciation of Nb in a low-tin ZIRLO irradiated to 63 MW d/kgU has been performed by X-ray absorption Spectroscopy and XRD using the microXAS beamline at Swiss Light Source (SLS).

The valuable possibility to perform experiments with a micro-focused beam and the choice of acquiring in parallel the XRF and XRD data using two detectors allowed obtaining high-resolution spectra in this study.

Results confirm that Nb retains a mostly metallic charge state in the vicinity of the metal-oxide interface with a gradual increase in the concentration of Nb^{2+} then Nb^{3+} with distance from the interface. The presence of Nb^{4+} and Nb^{5+} is observed at a distance of 1.6–2.2 micrometres from the metal-oxide interface of this alloy. This finding is important as the Nb in the oxide matrix also remains partly metallic in the very early stages of oxidation. Noteworthy amounts of Nb with a lower oxidation state than Nb^{4+} have been observed within the 'inner oxide' that is the first 1.6 μm and continue to exist further, in smaller quantities, into the oxide layer. The Nb oxidation starts gradually with the appearance of NbO, transitioning gradually to the fully oxidised Nb_2O_5 at a distance greater than 2 μm from the metal-oxide interface, for this alloy.

The XRD data show that close to the metal-oxide interface in the region where Nb is still metallic, the presence of tetragonal zirconia is relatively high. The study of this sample gives a hint towards the presence of a dense protective layer in the vicinity of the interface of this material with a higher tetragonal phase fraction and a large amount of unoxidised Nb. This inner layer has previously been described as a barrier layer and could act as a diffusion region. It is expected from the observation of the metal-oxide interface of other materials, that it also does not contain many interconnected cracks acting as rapid routes to the interface; meaning that ingressing species such as oxygen and hydrogen must diffuse through such a layer before reaching the underlying metal. Moreover, a noteworthy contribution of Nb in a less than 4+ state is found in the oxide matrix which is known to contribute towards the compensation of space charges reducing the hydrogen uptake for this material. It must be noted that the presence of higher concentration of tetragonal is not necessarily the main cause of this protectiveness, but rather, it could be a consequence of composition and microstructure of the oxide in that region.

Author statement

Jonathan Hawes: Methodology, Validation, Formal analysis, Investigation, Writing - Original Draft, Writing - Review & Editing, Visualization.

Peter Warnicke: Investigation, Writing - Original Draft, Methodology.

Patrick Burr: Validation, Formal analysis, Writing - Review & Editing.

Dario Ferreira Sanchez: Methodology, Data Curation, Visualization.

Daniel Grolimund: Resources, Writing - Review & Editing.

Jonna Partezana: Resources, Writing - Review & Editing.

Yu-Lung Chiu: Supervision, Writing - Review & Editing.

Sousan Abolhassani: Conceptualization, Methodology, Validation, Resources, Writing - Original Draft, Writing - Review & Editing, Visualization, Supervision, Project administration.

Declaration of Competing Interest

The authors declare that they have no known competing financial interests or personal relationships that could have appeared to influence the work reported in this paper.

Acknowledgements

The authors wish to acknowledge swissnuclear for the support of the HyUp research project, from financial and technical point of view. The sample has been provided by Westinghouse and within the frame of the MUZIC-3 working group activities. The authors acknowledge the sample preparation by Dr. Pia Tijeland and her team. Prof. Adrien Couet is acknowledged for the supply of NbO (2+) spectra. Mr Go Sajiki and Prof. Kiyotaka Asakura are thanked for the supply of Nb_2O_3 (3+) spectra. Sensitivity analysis of the quality of fit of the XANES results was performed with the assistance of resources and services from the Australian National Computational Infrastructure, MASSIVE, the Pawsey Supercomputing Centre and by Intersect Australia Ltd.

Appendix A

To investigate the sensitivity to the choice of energy range used for fitting, the fit was re-calculated iteratively using a progressively wider range of spectral energies. The start of the fitting range was kept constant at 18950 eV (i.e. just before the edge for the metallic Nb° standard), since the signal before the edge is not considered relevant to the fit, but would only add noise. On the other hand, the signal past the edge contains useful structure for fitting, but this is partly dependent on the local environment (which cannot be accounted for by the standards). Thus, we have considered a fitting range ending between 19000 eV and 19150 eV, with a step size of 2 eV.

The result of the sensitivity analysis, presented in Fig. A1, shows that curtailing the energy range too soon (<19050 eV) leads to significant uncertainties on the predicted concentrations of the Nb charge states. However, once the fitting is extended past 19050 eV, the predicted concentrations appear to converge for all points and become insensitive to further changes in the fitting range. For this reason, a fitting range of 18950–19070 eV was used for the analysis presented in this paper.

To characterize the quality-of-fit over the extended edge of the

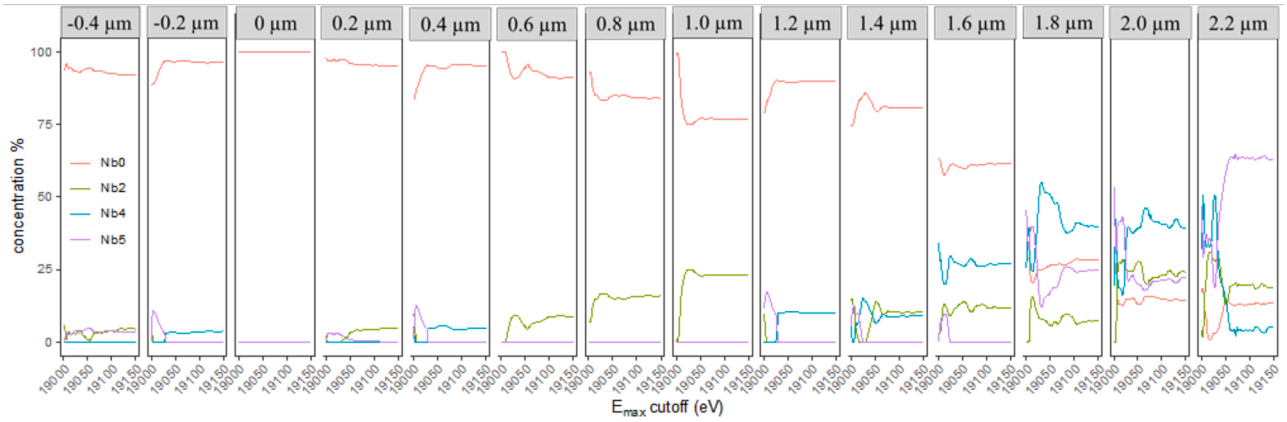

Fig. A1. Best-fit of four of the Nb standards to the measured XANES spectra as a function of fitting range end-point. The fitting range started at 18950 eV for all points, and ended between 19000 eV and 19150 eV, as per x-axis.

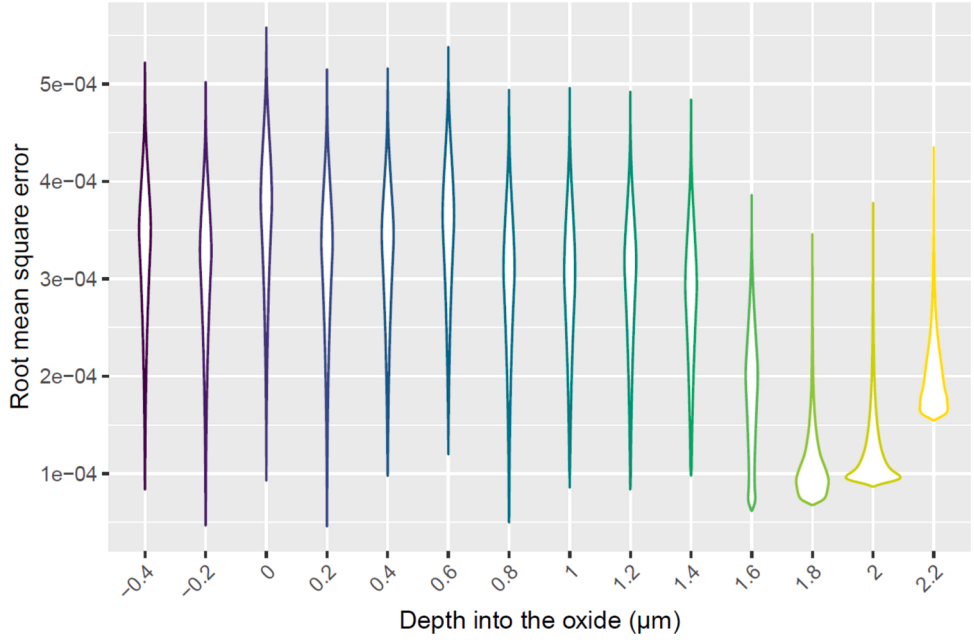

Fig. A2. Distribution of residual errors between model (linear combination of standard spectra) and measured spectra, when the fit is performed across all parameter space (i.e. for all allowed values of Nb^0, Nb^{2+}, Nb^{3+}, Nb^{4+} Nb^{5+} between [0,1]).

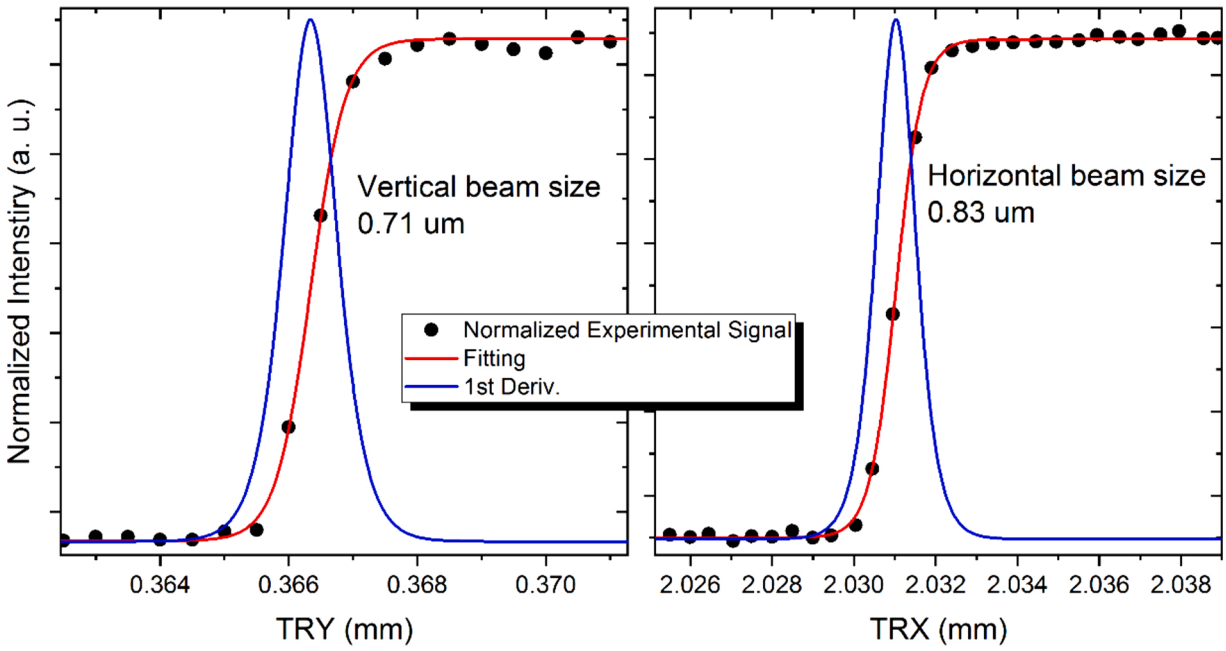

Fig. A3. Measured beam size for X-ray beam, in the vertical direction a diameter of 0.71 μm (FWHM) and in the horizontal direction 0.83 μm (FWHM).

XANES measurements, the fit was repeated across the entire compositional range. That is, the residual error (RMSE) of the fit was calculated for all possible combinations of fitting variables *a*, *b*, *c* and *d* in the range [0,1] with a step size of 0.01. In all cases, a single minimum is observed in the RMSE's five-dimensional parameter space. This provides reassurance that conventional optimisation algorithm should successfully identify the best-fit solution, irrespective of starting concentrations.

The distribution of residual errors for all possible fitting solutions, as shown in Fig. A2, provides insight on the uniqueness of the best-fit combination: for most points, the distribution of solution is sharp near the optimum, indicating that the best fit is in fact quite distinguishable from the other solutions. But in some cases, further into the oxide, the optimum becomes quite shallow, meaning that multiple solutions exist with different combinations of Nb standards but with similar residual error. By considering all solutions that yield a residual error that is within 0.1 % of the best fit RMSE (shaded areas in Fig. 5), we can identify those Nb oxidation states that are most sensitive to variations in the quality of fit. It is evident that in the metal and for most of the oxide, the variations in concentrations for solutions within 0.1 % of the optimum are small. They become larger for the last three points, deeper in the oxide, but at all points the uncertainty is reasonably small and does not affect the conclusions drawn.

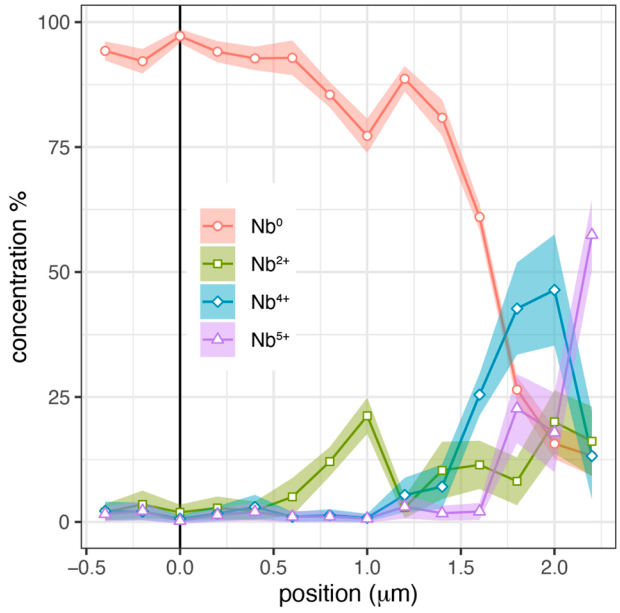

Fig. A4. The resulting constituent percentages for each position across the sample. The lines and points show the best linear combination fitting of the four reference standards. The shaded area represents the variation in fit when considering all solutions with residual error within 0.1 % of the best fit. Please refer to Fig. 5 for comparison with the same fit, using all five reference standards.

References

[1] T. Isobe, T. Murai, Y. Mae, Anodic protection provided by precipitates in aqueous corrosion of zircaloy, Zircon. Nucl. Ind. Elev. Int. Symp. (2009), https://doi.org/10.1520/stp16174s, pp. 203-203–15.

[2] C. Proff, S. Abolhassani, C. Lemaignan, Oxidation behaviour of zirconium alloys and their precipitates – a mechanistic study, J. Nucl. Mater. 432 (1–3) (2013) 222–238, https://doi.org/10.1016/j.jnucmat.2012.06.026.

[3] A. Couet, A.T. Motta, B. De Gabory, Z. Cai, Microbeam X-ray Absorption Near-Edge Spectroscopy study of the oxidation of Fe and Nb in zirconium alloy oxide layers, J. Nucl. Mater. 452 (1–3) (2014) 614–627, https://doi.org/10.1016/j.jnucmat.2014.05.047.

[4] A. Couet, A.T. Motta, R.J. Comstock, Effect of alloying elements on hydrogen pickup in zirconium alloys, Zircon. Nucl. Ind. 17th (2015) 479–514, https://doi.org/10.1520/STP154320120215.

[5] A.T. Motta, A. Couet, R.J. Comstock, Corrosion of zirconium alloys used for nuclear fuel cladding, Annu. Rev. Mater. Res. 45 (1) (2015) 311–343, https://doi.org/10.1146/annurev-matsci-070214-020951.

[6] A. Froideval, C. Degueldre, C.U. Segre, M.A. Pouchon, D. Grolimund, Niobium speciation at the metal/oxide interface of corroded niobium-doped Zircaloys: a X-ray absorption near-edge structure study, Corros. Sci. 50 (2008) 1313–1320, https://doi.org/10.1016/j.corsci.2008.01.011.

[7] A. Froideval, et al., Microprobe analysis of neutron irradiated and autoclaved zirconium niobium claddings using synchrotron-based hard X-ray imaging and spectroscopy, J. Nucl. Mater. 385 (2) (2009) 346–350, https://doi.org/10.1016/j.jnucmat.2008.12.022.

[8] S. Abolhassani, et al., Corrosion and hydrogen uptake in zirconium claddings irradiated in light water reactors, in: Zircon. Nucl. Ind. 17th Int. Symp. ASTM STP 1543, vol. 1543, 2015, pp. 540–573, https://doi.org/10.1520/STP154320130007.

[9] A. Couet, A.T. Motta, A. Ambard, The coupled current charge compensation model for zirconium alloy fuel cladding oxidation: I. Parabolic oxidation of zirconium alloys, Corros. Sci. 100 (2015) 73–84, https://doi.org/10.1016/j.corsci.2015.07.003.

[10] H.W.K. Une, K. Sakamoto, J. Matsunaga, Y. Etoh, M. Aomi, I. Takagc, K. Sawada, Controlling factors in hydrogen absorption of zirconium alloys, in: Manchester, UKProc. Topfuel 2012, vol. TopFuel-A0, 2012.
[11] H. Hulme, et al., An X-ray absorption near-edge structure (XANES) study of the Sn L3 edge in zirconium alloy oxide films formed during autoclave corrosion, Corros. Sci. 105 (2016) 202–208, https://doi.org/10.1016/j.corsci.2016.01.018.
[12] K. Sakamoto, K. Une, M. Aomi, K. Hashizume, Depth profile of chemical states of alloying elements in oxide layer of Zr-based alloys, Prog. Nucl. Energy 57 (2012) 101–105, https://doi.org/10.1016/j.pnucene.2011.12.012.
[13] G. Kuri, C. Degueldre, J. Bertsch, S. Abolhassani, Micro-focussed XAFS spectroscopy to study Ni-bearing precipitates in the metal of corroded Zircaloy-2, Appl. Phys. A Mater. Sci. Process. 98 (3) (2010) 625–633, https://doi.org/10.1007/s00339-009-5456-z.
[14] B. Ensor, A.M. Lucente, M.J. Frederick, J. Sutliff, A.T. Motta, The role of hydrogen in zirconium alloy corrosion, J. Nucl. Mater. 496 (2017) 301–312, https://doi.org/10.1016/j.jnucmat.2017.08.046.
[15] Y.P. Lin, O.T. Woo, Oxidation of β-Zr and related phases in Zr-Nb alloys: an electron microscopy investigation, J. Nucl. Mater. 277 (1) (2000) 11–27, https://doi.org/10.1016/S0022-3115(99)00153-1.
[16] S. Abolhassani, et al., TEM examinations of the metal-oxide interface of zirconium based alloys irradiated in a pressurized water reactor, J. ASTM Int. 2 (6) (2005) 12390, https://doi.org/10.1520/JAI12390.
[17] B. Ensora, Michael Moorehead, J.R. Seidensticker, A. Couet, A.T. Motta, XANES Study of Fe and Nb Oxidation in Zr-2.5Nb Oxide Layers Brendan Ensor, 2021, pp. 3–6.
[18] K. Sakamoto, K. Une, M. Aomi, T. Otsuka, K. Hashizume, Change of chemical states of niobium in the oxide layer of zirconium-niobium alloys with oxide growth, J. Nucl. Sci. Technol. 52 (10) (2015) 1259–1264, https://doi.org/10.1080/00223131.2015.1058196.
[19] M. Moorehead, Z. Yu, L. Borrel, J. Hu, Z. Cai, A. Couet, Comprehensive investigation of the role of Nb on the oxidation kinetics of Zr-Nb alloys, Corros. Sci. 155 (June) (2019) 173–181, https://doi.org/10.1016/j.corsci.2019.04.017.
[20] D. Franklin, C.-Y. Li, Effects of heat flux and irradiation-induced changes in water chemistry on zircaloy nodular oxidation, Zircon. Nucl. Ind. (2008), https://doi.org/10.1520/stp28120s, pp. 206-206–17.
[21] A. Grandjean, Y. Serruys, Metal and oxygen mobilities during Zircaloy-4 oxidation at high temperature, J. Nucl. Mater. 273 (1) (1999) 111–115, https://doi.org/10.1016/S0022-3115(99)00036-7.
[22] A. Yilmazbayhan, A.T. Motta, R.J. Comstock, G.P. Sabol, B. Lai, Z. Cai, Structure of zirconium alloy oxides formed in pure water studied with synchrotron radiation and optical microscopy: relation to corrosion rate, J. Nucl. Mater. 324 (1) (2004) 6–22, https://doi.org/10.1016/j.jnucmat.2003.08.038.
[23] A.T. Motta, et al., Microstructure and growth mechanism of oxide layers formed on Zr alloys studied with micro-beam synchrotron radiation, in: Zircon. Nucl. Ind. 14th Int. Symp., vol. 1467, 2005, pp. 205–232, https://doi.org/10.1520/stp37508s, no. 5.
[24] N. Pétigny, P. Barberis, C. Lemaignan, C. Valot, M. Lallemant, In situ XRD analysis of the oxide layers formed by oxidation at 743 K on Zircaloy 4 and Zr-1NbO, J. Nucl. Mater. 280 (3) (2000) 318–330, https://doi.org/10.1016/S0022-3115(00)00051-9.
[25] Aylin Yilmazbayhan, Microstructural Basis of Uniform Corrosion in ZR Alloys, Pennsylvania State University, 2004.
[26] E. Polatidis, et al., Residual stresses and tetragonal phase fraction characterisation of corrosion tested Zircaloy-4 using energy dispersive synchrotron X-ray diffraction, J. Nucl. Mater. 432 (1–3) (2013) 102–112, https://doi.org/10.1016/j.jnucmat.2012.07.025.
[27] M. Chollet, et al., Synchrotron X-ray diffraction investigations on strains in the oxide layer of an irradiated Zircaloy fuel cladding, J. Nucl. Mater. 488 (2017) 181–190, https://doi.org/10.1016/j.jnucmat.2017.03.010.
[28] A. Garner, A. Gholinia, P. Frankel, M. Gass, I. Maclaren, M. Preuss, The microstructure and microtexture of zirconium oxide films studied by transmission electron backscatter diffraction and automated crystal orientation mapping with transmission electron microscopy, Acta Mater. 80 (2014) 159–171, https://doi.org/10.1016/j.actamat.2014.07.062.
[29] S. Abolhassani, P. Gasser, Preparation of TEM samples of metal-oxide interface by the focused ion beam technique, J. Microsc. 223 (1) (2006) 73–82, https://doi.org/10.1111/j.1365-2818.2006.01599.x.
[30] K. Asakura, H. Abe, M. Kimura, The challenge of constructing an international XAFS database, J. Synchrotron Radiat. 25 (4) (2018) 967–971, https://doi.org/10.1107/S1600577518006963.
[31] G. Sajiki, Y. Benino, C. Oki, K. Ohara, H. Okano, T. Nanba, Structural analyses and reverse Monte Carlo modeling of niobium oxide amorphous film prepared by sputtering method, J. Ceram. Soc. Jpn. 125 (10) (2017) 760–765, https://doi.org/10.2109/jcersj2.17053.
[32] R.C. Garvie, P.S. Nicholson, Phase analysis in zirconia systems, J. Am. Ceram. Soc. 55 (6) (1972) 303–305, https://doi.org/10.1111/j.1151-2916.1972.tb11290.x.
[33] J.R. Taylor, An Introduction to Error Analysis, University Science Books Sausalito, California, 1997, pp. 87–88.
[34] S. Abolhassani, C. Proff, L. Veleva, T.M. Karlsen, P. Bennett, B. Oberla, Transmission electron microscopy examinations of metal-oxide interface of zirconium-based alloys irradiated in Halden, Zircon. Nucl. Ind. 18th Int. Symp. (2018) 614–644, https://doi.org/10.1520/STP159720160039.
[35] J. Hu, et al., Understanding corrosion and hydrogen pickup of zirconium fuel cladding alloys: the role of oxide microstructure, porosity, suboxides, and second-phase particles, Zircon. Nucl. Ind. 18th Int. Symp. (2018) 93–126, https://doi.org/10.1520/stp159720160071.
[36] B.D.C. Bell, et al., The influence of alloying elements on the corrosion of Zr alloys, Corros. Sci. 105 (2016) 36–43, https://doi.org/10.1016/j.corsci.2015.12.022.
[37] B.D.C. Bell, S.T. Murphy, R.W. Grimes, M.R. Wenman, The effect of Nb on the corrosion and hydrogen pick-up of Zr alloys, Acta Mater. 132 (2017) 425–431, https://doi.org/10.1016/j.actamat.2017.04.063.
[38] Z. Yu, A. Couet, M. Bachhav, Irradiation-induced Nb redistribution of ZrNb alloy: an APT study, J. Nucl. Mater. 516 (2019) 100–110, https://doi.org/10.1016/j.jnucmat.2019.01.015.
[39] K. Une, et al., Hydrogen absorption mechanism of zirconium alloys based on characterization of oxide layer, J. ASTM Int. 8 (5) (2011) 401–432, https://doi.org/10.1520/JAI102950.
[40] B. Cox, Pore structure in oxide films on irradiated and unirradiated zirconium alloys, J. Nucl. Mater. 148 (3) (1987) 332–343, https://doi.org/10.1016/0022-3115(87)90027-4.
[41] G. Sundell, M. Thuvander, H.O. Andrén, Barrier oxide chemistry and hydrogen pick-up mechanisms in zirconium alloys, Corros. Sci. 102 (2015) 490–502, https://doi.org/10.1016/j.corsci.2015.11.002.
[42] J. Hu, et al., Hydrogen pickup during oxidation in aqueous environments: the role of nano-pores and nano-pipes in zirconium oxide films, Acta Mater. 180 (2019) 105–115, https://doi.org/10.1016/j.actamat.2019.09.005.
[43] N. Ni, S. Lozano-Perez, J.M. Sykes, G.D.W. Smith, C.R.M. Grovenor, Focussed ion beam sectioning for the 3D characterisation of cracking in oxide scales formed on commercial ZIRLOTM alloys during corrosion in high temperature pressurised water, Corros. Sci. 53 (12) (2011) 4073–4083, https://doi.org/10.1016/j.corsci.2011.08.013.
[44] L. Kurpaska, I. Jozwik, J. Jagielski, Study of sub-oxide phases at the metal-oxide interface in oxidized pure zirconium and Zr-1.0% Nb alloy by using SEM/FIB/EBSD and EDS techniques, J. Nucl. Mater. 476 (2016) 56–62, https://doi.org/10.1016/j.jnucmat.2016.04.038.
[45] K.J. Annand, I. Maclaren, M. Gass, Utilising DualEELS to probe the nanoscale mechanisms of the corrosion of Zircaloy-4 in 350°C pressurised water, J. Nucl. Mater. 465 (2015) 390–399, https://doi.org/10.1016/j.jnucmat.2015.06.022.
[46] J. Hu, et al., Identifying suboxide grains at the metal-oxide interface of a corroded Zr-1.0%Nb alloy using (S)TEM, transmission-EBSD and EELS, Micron 69 (2015) 35–42, https://doi.org/10.1016/j.micron.2014.10.004.
[47] B. De Gabory, A.T. Motta, K. Wang, Transmission electron microscopy characterization of Zircaloy-4 and ZIRLOTM oxide layers, J. Nucl. Mater. 456 (2015) 272–280, https://doi.org/10.1016/j.jnucmat.2014.09.073.
[48] N. Ni, et al., How the crystallography and nanoscale chemistry of the metal/oxide interface develops during the aqueous oxidation of zirconium cladding alloys, Acta Mater. 60 (20) (2012) 7132–7149, https://doi.org/10.1016/j.actamat.2012.09.021.
[49] R.J. Nicholls, et al., Crystal structure of the ZrO phase at zirconium/zirconium oxide interfaces, Adv. Eng. Mater. 17 (2) (2015) 211–215, https://doi.org/10.1002/adem.201400133.